Epitaxial La0.5Sr0.5MnO3-δ Bipolar Memristive Devices with Tunable and Stable Multilevel States

Carlos Moncasi, Gauthier Lefèvre, Quentin Villeger, Laetitia Rapenne, Thoai-khanh Khuu, Fabrice Wilhelm, Andrei Rogalev, Carmen Jiménez, Mónica Burriel

RESEARCH ARTICLE

ADVANCED MATERIALS INTERFACES
Open Access
www.advmatinterfaces.de

Epitaxial $La_{0.5}Sr_{0.5}MnO_{3-\delta}$ Bipolar Memristive Devices with Tunable and Stable Multilevel States

*Carlos Moncasi, Gauthier Lefèvre, Quentin Villeger, Laetitia Rapenne, Thoai-Khanh Khuu, Fabrice Wilhelm, Andrei Rogalev, Carmen Jiménez, and Mónica Burriel**

Valence change memories are novel data storage devices in which the resistance is determined by a reversible redox reaction triggered by voltage. The oxygen content and mobility within the active materials of these devices play a crucial role in their performance. Therefore, materials which present fast oxygen migration properties and can accommodate variable oxygen stoichiometry are promising candidates. In this work, the perovskite $La_{0.5}Sr_{0.5}MnO_{3-\delta}$ (LSM50) as memristive material is studied, which presents a more facile oxygen vacancy formation and faster oxygen migration compared to other strontium-substituted manganites. For the first time reproducible resistive switching is reported in epitaxial LSM50-based devices with active Ti electrodes, which show large operating window and stable multilevel states. Based on the structural, chemical, and electrical results, a simple phenomenological description of the resistive switching phenomena taking place in these novel LSM50-based memristive devices is proposed.

1. Introduction

In the era of information, the last years have shown that our society evolves towards digitalization, where many professional and nonprofessional interactions are made through a screen. These interactions involve a large amount of data and power consumption that keep raising as society asks for more content, better quality, faster operation, and better energy efficiency. One of the latest and hottest sources of data production is related to artificial intelligence (AI), which aims to mimic the outstanding performance of the human brain. AI is mostly performed by means of silicon-based technology and hardcoded software, which is extremely energy-demanding. All in all, the amount of data is rapidly scaling up and so does its storage and energy consumption.

In parallel to the raising of data generation, research, and industry keep looking for novel approaches to improve the performance of silicon technology. Among the variety of approaches proposed in the research-focused group "Beyond CMOS", by International Roadmap for Devices and Systems,[1] resistive switching (RS) phenomena holds the promise to overcome the limitations faced by silicon technology. In RS, the reversible change of resistance in a device between a high resistance state (HRS) and a low resistance state (LRS) is exploited to store the information, as for the regular binary storage. RS has been previously reported in a large sort of materials,[2] where depending on the materials' properties and the electrodes, the change of resistance can have different phenomenological origins.[3–7] In the case of valence change memories (VCMs), the change of resistance is related to the variable oxygen content and the concomitant change of valence in the cationic sublattice, which ultimately modifies the resistivity of the material.[8,9] Moreover, some VCMs show analog multilevel resistance, which increases the storage density per device while minimizing the space required for storing data.[3,10] On top of that, VCMs can be used for neuromorphic computing, where the device itself shows the behavior that is typically hardcoded in most AI applications, and hence, VCMs may present larger storage density and lower power consumption in applications such as those involving AI.[11–13]

In our previous work, we studied pure $LaMnO_{3+\delta}$, and proved that it was possible to change the resistance state up to two orders of magnitude by oxygen drift and by the concomitant redox reactions taking place at the materials' surface, as experimentally proven by combining conductive atomic force microscopy with X-ray photoemission electron spectroscopy

C. Moncasi, Q. Villeger, L. Rapenne, T.-K. Khuu, C. Jiménez, M. Burriel
Univ. Grenoble Alpes
CNRS
Grenoble INP
LMGP
Grenoble 38000, France
E-mail: monica.burriel@grenoble-inp.fr
G. Lefèvre
Univ. Grenoble Alpes
CEA
LITEN
Grenoble 38000, France
F. Wilhelm, A. Rogalev
ESRF
The European Synchrotron
Grenoble 38043, France

The ORCID identification number(s) for the author(s) of this article can be found under https://doi.org/10.1002/admi.202202496.

DOI: 10.1002/admi.202202496

and Raman spectroscopy.[14] This material was further used to build memristive devices with noble metal electrodes (Au and Pd),[15,16] as well as an active oxidizable electrode, such as TiN,[17] and to study the switching mechanisms taking place for the different types of electrodes. We then extended our work to Sr-substituted manganites, and we found that the performance of $La_{0.8}Sr_{0.2}MnO_{3\pm\delta}$ (LSM20)-based memristive devices is improved by the presence of extended structural defects, which act as fast oxygen migration pathways.[3] Having in mind that the oxygen transport properties in $La_{1-x}Sr_xMnO_3$ (LSM) are influenced by the stoichiometry and the composition,[18–21] in the present work we focus on $La_{0.5}Sr_{0.5}MnO_{3-\delta}$ (LSM50) to study the effect of using a more easily reducible composition, with a larger oxygen off-stoichiometry window (δ), on the performance of memristive devices.[22] While the RS performance depends on many material properties and device parameters, for ease of comparison the geometry of the devices and the electrode material for LSM50 devices are the same as those previously reported for LSM20.[3] In LSM50, the La^{3+} substitution by Sr^{2+} is typically accommodated by the oxidation of Mn^{3+} into Mn^{4+}, which creates an electron-hole, and formation of oxygen vacancies (δ).[22–24] According to Mizusaki et al.[22] and supported by computational works,[25,26] the formation of oxygen vacancies in LSM50 is more favored than in any other Sr substituted LSM composition, in agreement with the differences in tracer bulk diffusion coefficient (10^{-16} cm^2 s^{-1} and 2×10^{-15} cm^2 s^{-1} for LSM20 and LSM50 at 700 °C, respectively).[27,28] As reported by Mizusaki et al.,[22] oxygen-stoichiometric LSM50 ($\delta = 0$) lays on the edge between p-type and n-type conductivity, but the presence of oxygen vacancies will turn it into p-type conductor. Due to the large electron-hole concentration, LSM50 presents a higher conductivity than any other Sr-substituted LSM compositions,[22,29,30] for which the homogeneous distribution of electric field within the material is expected to favor an interface-type memristive response, preventing the dielectric breakdown typical of filamentary-type RS.[31] As suggested by Choi et al.,[32] who studied polycrystalline LSM vertical devices with $x = 0.1$, 0.3, and 0.5, larger operating windows are expected as the Sr content increases (in the studied range of $x = 0.1$–0.5). Nonetheless, the authors observed a narrowing of the HRS/LRS window from $x = 0.3$ to $x = 0.5$ which was ascribed to a poor crystallization of the LSM50 film. Asanuma et al.[33] studied the effect of cation substitution $Pr_{1-x}Ca_xMnO_{3\pm\delta}$ (PCMO) with $x = 0$–1 (similar system to LSM) in the memristive properties of vertical Ti/PCMO/$SrRuO_3$ devices. The authors observed the presence of an amorphous TiO_x interlayer, which thickness increases during operation, and reduced PCMO at the interface, which increases the band gap. The change in the band diagram induced by Ca substitution (which increases the work function, and has the smallest band gap for $x \approx 0.5$) and oxygen vacancies (which increases the band gap) was ascribed to the RS performance observed, for which the largest HRS/LRS ratio was measured for $x \approx 0.4$. Therefore, according to these previous studies, a large operating window is expected for LSM50 compared to LSM compositions with lower oxygen vacancy concentration, for devices with the same type of Ti electrodes, and for fixed thickness and microstructure.

The memristive properties of LSM50 are studied using titanium as an active electrode. As for other material combinations,[3,11,13,33–39] the Ti/LSM50 stack can undergo a reversible redox reaction that originates two additional interlayers: oxidized metal electrode and oxygen-deficient oxide. The resistivity of both interlayers is higher than the parent compound. Hence, the resistance of the device is expected to respond to the interplay of the two reaction interlayers.

2. Results

2.1. Structural Characterization of Epitaxial LSM50

A 21 nm thick film of $La_{0.5}Sr_{0.5}MnO_{3-\delta}$ (LSM50), as measured by X-ray Reflectometry (XRR, see Figure S1), was grown by Pulsed injection metal-organic chemical vapor deposition (PI-MOCVD) on a $(001)_{pc}$-oriented $LaAlO_3$ (LAO) substrate. The deposition technique and conditions have been described elsewhere[3] and are summarized in the Experimental Section. As shown in the X-ray difraction (XRD) pattern, presented in

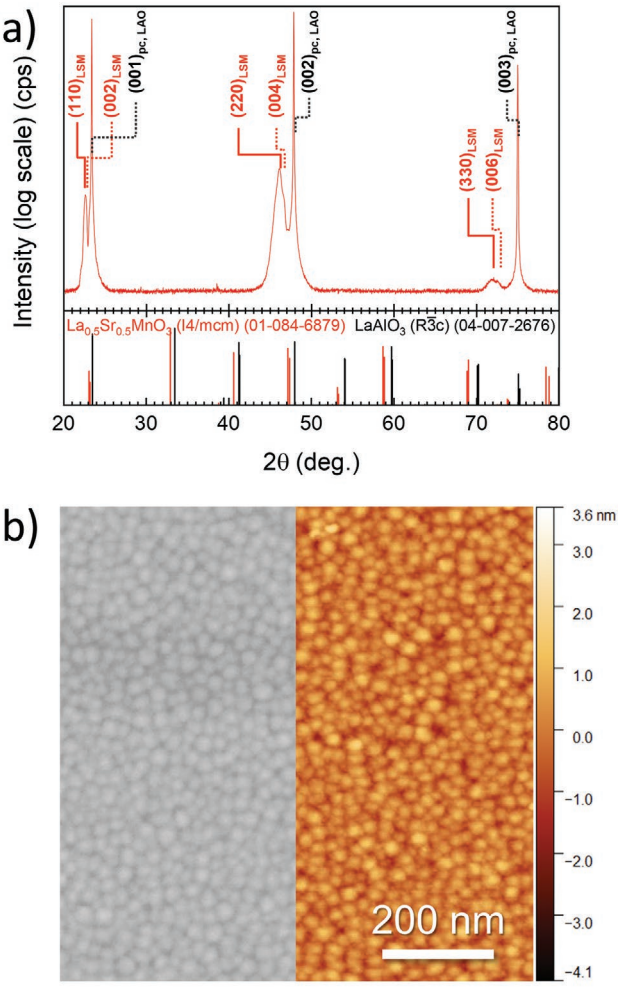

Figure 1. a) XRD θ-2θ patterns of the LSM50/LAO film. Diffraction peaks of LAO are indexed in pseudo-cubic (pc) notation. The bottom panel displays the database reference for LSM50 and LAO. b) Surface morphology of the LSM50/LAO film observed by SEM (left) and AFM (right) with common scale.

Figure 1a, obtained in Bragg–Brentano configuration, besides the reflections from the LAO substrate, only the LSM50 (*hh*0) and (00*l*) reflections are observed. These reflections correspond to a pseudocubic (00*l*) orientation, and hence, suggest an oriented growth of the LSM50 film. Using the cell parameters of LSM50 ($a = b = 5.451$ Å, and $c = 7.675$ Å, from ICDD-PDF 01-084-6879), the theoretical in-plane distance between two consecutive Mn in the (00*l*)-oriented domain is $d_{[001]LSM50} = a/\sqrt{2} = 3.854$ Å, and in the domain (*hh*0) it is $d_{[110]LSM50} = c/2 = 3.838$ Å. Therefore, the (00*l*)- and (*hh*0)-oriented domains in LSM50/LAO present different compressive in-plane strain, $\varepsilon_{[001]} = -1.67\%$ and $\varepsilon_{[110]} = -1.24$ %, respectively. Considering the pseudocubic cell parameters of LSM50 ($a_{pc} = 3.854$ Å and $c_{pc} = 3.838$ Å) and LAO ($a_{pc} = 3.794$ Å and $c_{pc} = 3.785$ Å), the average cell parameter of the two domains measured by XRD ($c_{pc} = 3.93 \pm 0.01$ Å) indicates an elongation of the cell along the out-of-plane direction ($\varepsilon_{zz} = +2\%$) due to the in-plane strain induced by the substrate, in a similar manner as the growth of $La_{0.8}Sr_{0.2}MnO_{3\pm\delta}$/LAO films.[3,40]

The observation of the surface morphology by Scanning Electron Microscopy (SEM) and Atomic Force Microscopy (AFM), as presented in Figure 1b, shows that the film is dense and flat (root mean square roughness of $S_q = 0.5$ nm), and with no pinholes, which makes it suitable for resistive switching applications. The layer is composed of homogeneously-distributed nanometric-size grains of 27 ± 3 nm (Stranski–Krastanov growth mode), possibly related to the crystal domains mentioned above.

The crystalline quality of the film was evaluated by Transmission Electron Microscopy (TEM), by cross-section observation, which corroborated the thickness measured by XRR. The film is homogeneous and with long-range atomic order, as observed in the TEM cross-section image of LSM50[001]/LAO[001] (**Figure 2**a). The overlapping diffraction spots of LSM50 and LAO in the selective area electron diffraction (SAED) carried out at the LSM50/LAO interface (Figure 2b) confirms the epitaxial growth of the LSM50 film on the LAO substrate. Microstructural insights were attained by performing the Fourier transform (FT) of the image in Figure 2a, as shown in the inset of Figure 2c, followed by a masking on the $(010)_{LSM,\ LAO}$ of the FT to obtain the inversed Fourier transform image (FT^{-1}), presented in Figure 2c. Only the diffraction planes perpendicular to the interface are visible on the FT^{-1} image, and they extend from the substrate interface to the film surface, demonstrating the very good crystal quality of the film. Nonetheless, as presented in the zoomed area in Figure 2c, some of the planes deflect and some extra planes appear, i.e., dislocations, at thicknesses >10 nm. Both phenomena may be related to the strain induced by the substrate. Summarizing, the morphology and microstructure of LSM50/LAO film are suitable for device micro-fabrication and allow to evaluate for the first time the memristive properties of epitaxial LSM50 thin films.

2.2. Electrical Characterization of LSM50 Memristive Devices

Planar LSM50-based memristive devices were micro-fabricated. Each device is composed of two facing square electrodes deposited on top of the LSM50 film. The inert electrode is composed of a 100 nm thick Pt layer, while the active electrode is composed of a bilayer of 10 nm of Ti capped with 90 nm thick Pt layer, as sketched in Figures S2 and S3, Supporting Information. Devices with different electrode contact sizes were fabricated to study the memristive response. A scheme of the devices is presented in Figure S2. In addition, an array of Pt electrodes separated at different distances were microfabricated to perform transmission line measurements (TLM), from which the resistivity of the epitaxial LSM50 film (1.6×10^{-3} Ωcm) and the Pt/LSM50 contact resistivity (3.0×10^{-2} Ωcm^2) were obtained. The resistivity measured lies in the upper half of the values reported in literature ($0.1 \times 10^{-3} - 17 \times 10^{-3}$ Ωcm),[41,42] which values widely depend on the processing technique and microstructure. This relatively high LSM50 resistivity value could suggest the presence of oxygen vacancies in the layer,[22] yet the influence of strain cannot be ruled out.[43–45]

2.2.1. Initial Resistance State

The initial resistance state (IRS) of the planar Ti/LSM50\Pt memristive devices was measured at +0.1 V. The IRS is inversely proportional to the contact area (3.0×10^3 Ω and 0.8×10^3 Ω for $A = 100^2$ and 400^2 μm^2, respectively, see Figure S2, Supporting Information) with a slope of –0.5, which suggests that the IRS is not solely governed by the electrode/LSM50 interface (expected slope of –1). As explained in detail in the Supporting Information and in Figure S3, Supporting Information, a slope of –0.5 can be attributed to the series resistance

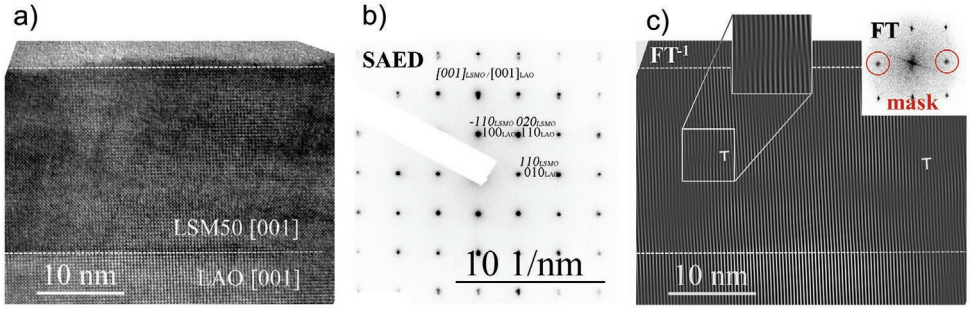

Figure 2. a) TEM cross-section image of 21 nm thick LSM50/LAO film. b) Selective area electron diffraction at the LSM50/LAO interface. c) Fourier transform (FT) of a) and inverse Fourier transformed image (FT^{-1}) obtained by applying the mask on (010) LSM50, LAO. Dislocations are marked with the symbol "T" in c).

contribution of the LSM50 film between the electrodes being the major contribution governing the IRS size dependence.

An electron transparent lamella of the Pt/Ti/LSM50 stack was obtained by Focused Ion Beam (FIB) in a pristine device and was then observed by STEM-EDS. The stack presents a partially oxidized amorphous TiO_x interlayer, with oxygen accumulation at the Ti/LSM50 interface, which then gradually decreases across the Ti electrode (discussed later). A similar EDS profile was observed for pristine Ti/LSM20\Pt memristive devices in our previous study,[3] in which the as-fabricated devices presented a narrow TiO_x interlayer, and a lower Mn oxidation state of the LSM20 layer under the Ti electrode, compared to electrode-free regions, as probed by X-ray absorption near edge spectroscopy (XANES) (see Figure S4, Supporting Information). Mizusaki et al.[22] showed that LSM50 is more prompt to be reduced (to lose oxygen ions) than other LSM compositions with lower Sr content. Therefore, considering that the electrodes are evaporated at room temperature and under high vacuum conditions (≈10^{-8} mbar), we propose that, similar to our previous work, during fabrication of the devices, part of the oxygen ions of the LSM50 layer migrate into the Ti electrode causing the further reduction of LSM50 and the oxidation of Ti, resulting both phenomena in an increase of the material's resistivity.

2.2.2. Memristive Response of the Ti/LSM50\Pt Devices

The Ti/LSM50\Pt devices exhibit memristive response without the need of an electroforming step. For the standard devices, with electrodes of $A = 200^2$ μm^2 and distance between electrodes of $L = 50$ μm, resistive switching was observed in 95% of the devices. In order to study the cycle-to-cycle variability and the writing voltage dependence, the following initialization procedure was carried out: five symmetrical voltage sweeps, $0 \rightarrow +V_{amp} \rightarrow 0 \rightarrow -V_{amp} \rightarrow 0$ for each V_{amp}, where the V_{amp} was increased from 2 to 12 V and then decreased symmetrically down to 2 V. During the application of voltage, the current was measured and the resistance was calculated as the ratio of voltage over current, known as static resistance. The static resistance-voltage (*R-V*) curves for increasing and decreasing V_{amp} are presented in **Figure 3**a,b, respectively. The devices show analog-type switching with counter-clockwise *R-V* characteristics for the complete range of voltage amplitudes tested (clear hysteresis for V_{amp} greater than 2 V). During the positive voltage increase, the measured static resistance gradually increases for voltages greater than 2 V. After the positive half-loop, the resistance increased by one order of magnitude. It can be thus concluded that the device has undergone a RESET and switched to HRS. On the contrary, when the absolute voltage is increased in negative polarity, the *R-V* curves show small stepwise drops of resistance, which recall multifilament-like switching. In this case, the device has undergone a SET operation and LRS is attained. The decrease in resistance (SET operation) appears at larger absolute voltage as the HRS value increases (V_{amp} increases). We note that the operation of the devices was limited to 12 V, as larger field caused an irreversible increase of resistance. Interestingly, the LRS values (measured close to 0 V) of the initialized device (≈145 kΩ for V_{amp} = 2 V, Figure 3b) are larger than those of the pristine device

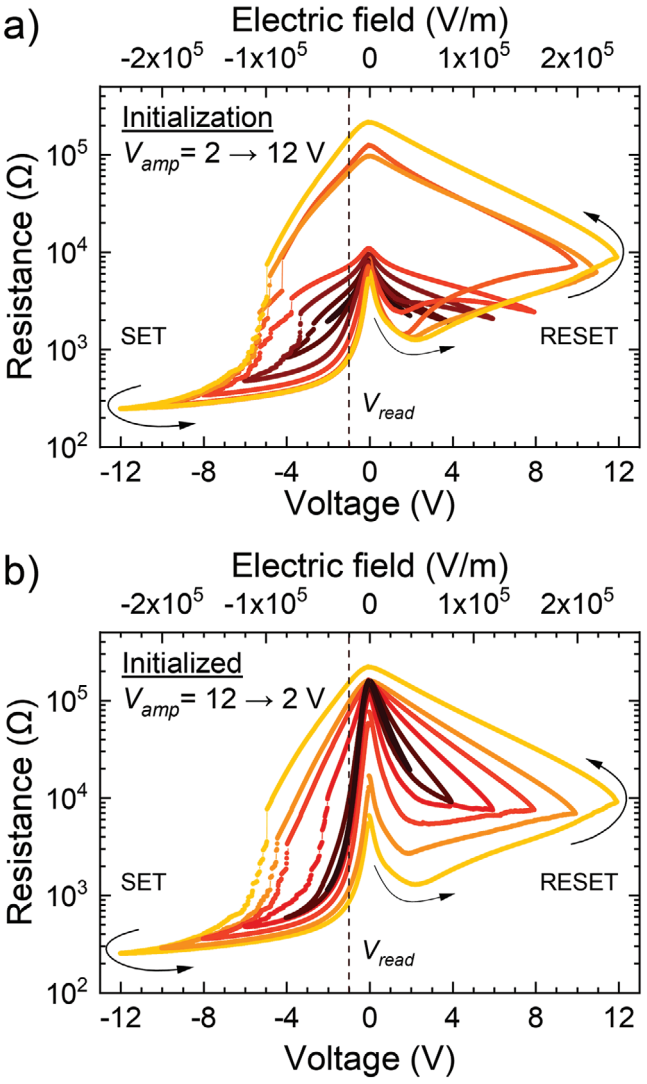

Figure 3. Static resistance-voltage curves of a standard Pt/Ti/LSM50\Pt device a) during the initialization $V_{amp} = 2 \rightarrow 12$ V and b) once initialized for $V_{amp} = 12 \rightarrow 2$ V. The dashed line corresponds to the reading voltage used to measure the resistance states, i.e., $V_{read} = -1$ V.

(≈7 kΩ for V_{amp} = 2 V, Figure 3a), which suggests that the equilibrium conditions of an initialized device correspond to a higher resistance. The device is considered initialized once it reaches the maximum voltage amplitude of operation. From that instant on, reproducible switching is observed. The HRS and LRS of the complete initialization procedure as function of cycles and writing voltage are presented in **Figure 4**a as open symbols, where the resistance states were extracted from the *R-V* curves at −1 V, as marked in Figure 3. For simplicity, as no clear switching voltage can be defined (for the SET and particularly for the RESET), we refer to the writing voltage as the voltage amplitude of the DC sweep. During the initialization at increasing V_{amp} (cycle 1–35 in Figure 4a) the LRS/HRS pairs depend on the writing voltage amplitude monotonically decreasing/increasing for $V_{amp} \leq 8$ V, followed by a sudden increase at 10 V during the first RESET operation, reaching a relatively high HRS. Then, the HRS increases further when

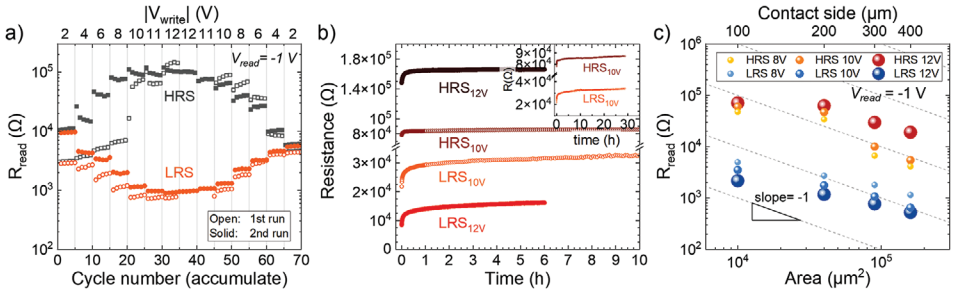

Figure 4. a) Resistance states evolution with symmetric voltage cycles (bottom axis) and writing voltage dependence (top axis). Open symbols correspond to the initialization of the device (first run). The symmetric voltage cycling procedure was carried out a second time to assess the reproducibility, represented by solid symbols. b) HRS_{10V}, HRS_{12V}, LRS_{10V}, and LRS_{12V} retention for a Pt/Ti/LSM50\Pt device programmed at V_{amp} = 10 V and 12 V. The inset shows the long-term evolution of the states programmed at V_{amp} = 10 V The resistance was measured at +0.1 V. c) Area dependence of the HRS and LRS resistance-states programmed at the different voltage for devices with electrode contact area of 100^2, 200^2, 300^2, and 400^2 μm^2.

writing using a voltage of 12 V, for which an HRS/LRS ratio larger than two orders of magnitude is achieved (HRS/LRS = 184 ± 6). Next, once the device is initialized, both HRS and LRS can be finely tuned by adjusting the writing voltage. The increasing/decreasing amplitude cycling procedure was repeated, including this time cycles at 11 and 12 V, and the resistance states measured are represented as solid symbols in Figure 4a. In the second repetition, the HRS and LRS exhibit the same trend of the initialized device (cycle 35–70 open symbols in Figure 4a), a smaller cycle-to-cycle variability (particularly for the LRS), and slightly smaller operating window (HRS/LRS = 108 ± 6 at V_{amp} = 12 V).

The stability over time (retention) of four multistates was measured in a different standard device, which was initialized as described above and shows comparable switching behavior. The device was programmed at a HRS_{10V} (LRS_{10V}) state at V_{write} = +10 (–10 V) and at a HRS_{12V} (lower LRS_{12V}) at V_{write} = +12 (–12 V). The resistance states programmed at 10 V (12 V) were measured at +0.1 V for nearly 30 h (6 h), as presented in Figure 4b. The four resistance states (HRS and LRS) experience an increase of resistance during the first 5 min, that gradually leads towards a constant value over time. This behavior suggests again that the device tends to stabilize at larger resistance values than the initial one. The four resistance states are clearly distinguishable over the total measured time. These devices also present a good reproducibility at high operating voltages. Reproducible HRS and LRS were obtained for at least 50 and 25 cycles at V_{amp} = 10 V and 12 V, respectively, in another device (see Figure S5, Supporting Information). Therefore, we conclude that initialized memristive devices based on epitaxial LSM50 show analog-type switching, multilevel states with a good retention and reproducible performance with large operating windows, that can be conveniently adjusted depending on the selected V_{amp}.

The effect of changing the electrode contact area, A, was also studied. Devices with square electrodes of A = 100^2, 300^2, and 400^2 μm^2 (L = 50 μm) show similar R-V characteristics and multilevel capabilities than the standard devices (A = 200^2 μm^2). The R-V curves of an initialized device with A = 300^2 and 400^2 μm^2 are presented in Figure S6, Supporting Information, where the jumps of resistance occurring during the SET transition are smaller and are closer to an apparent gradual transition. Figure 4c presents the HRS and LRS programmed at different writing voltage amplitudes for the devices with A = 100^2 to 400^2 μm^2. The different HRS of the larger devices (A = 200^2 – 400^2 μm^2) scale with the area, as expected for an interface-type resistive switching, while the small 100^2 μm^2 devices slightly deviate from this trend. On the other hand, the LRS presents a slope ≈–0.5 which suggests a weaker dependence with the area and thus, with the Ti/LSM50 resistance. In this LRS state, the resistance is dominated by the 50 μm long LSM50 between the electrodes (see Supporting Information for the interpretation of the slope in R vs A).

2.2.3. Chemical and Microstructural Changes of the Ti/LSM50\Pt Devices After Operation

The chemical profile across the Pt/Ti/LSM50/LAO stack obtained in the center of the electrode in a device in pristine, HRS_{12V}, and LRS_{12V} state was measured by STEM-EDS, as presented in **Figure 5**. While the composition of LSM50 remains

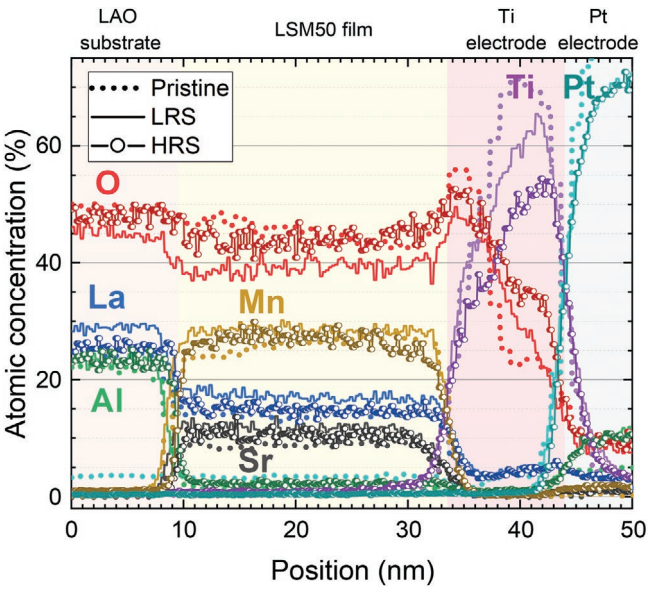

Figure 5. STEM-EDS chemical profiles across the Pt/Ti/LSM50/LAO stacks of a memristive device in pristine, LRS, and HRS state. The chemical profiles were obtained over an area of 60 nm with integrated thickness of 70 nm.

ADVANCED MATERIALS INTERFACES
Open Access
www.advmatinterfaces.de

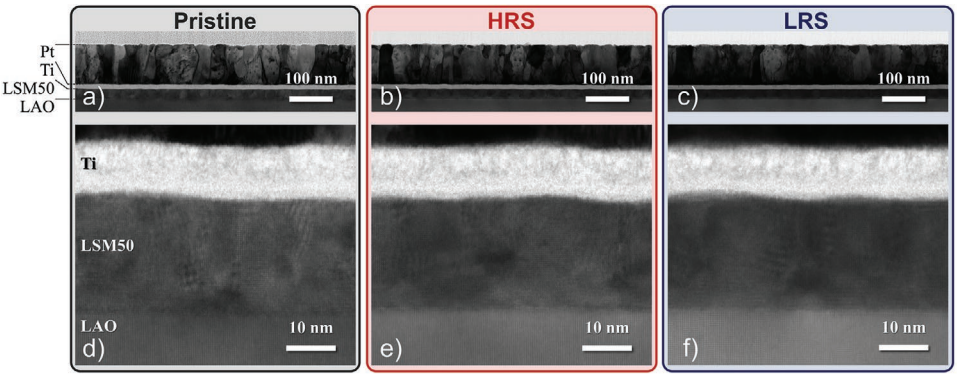

Figure 6. TEM images of the Pt/Ti/LSM50/LAO stacks obtained in devices in a), d) pristine, b), e) HRS_{12V} and c), f) LRS_{12V} state.

similar in both resistance states, the HRS stack presents a slightly broader and oxygen-richer TiO_x interlayer. The oxygen content in the Ti electrode has increased upon voltage operation, where the TiO_x interlayer is thicker than in the pristine state. As shown in **Figure 6**, the high crystal quality and epitaxy of the film in pristine state is maintained for the films in HRS_{12V} and LRS_{12V}.

However, it should be noted that at the edge of the Ti electrode side facing the opposite electrode, the cycled devices present a region ≈400 nm long of amorphous LSM50 (a-LSM50), 100 nm of which are under the Ti electrode, as shown in Figure S7, Supporting Information, for HRS_{12V} and LRS_{12V}. Contrary to the cycled devices, the pristine ones showed no amorphous LSM50 phase. A slightly lifted Pt/Ti electrode edge is present already in the pristine state (Figure S7h, Supporting Information), which we infer is inherent to the microfabrication process and not to the voltage operation of the device. The amorphous region in the cycled devices is characterized by a lack of atomic order, the presence of voids with variable size, which appear darker in the TEM images, and the apparent increase of thickness and surface roughness. No substantial chemical changes were found for La, Mn, and Sr along the a-LSM50 region compared to the crystalline LSM50, as presented in Figure S7, Supporting Information, while the oxygen concentration clearly increases. Similar characteristics were found in the LRS devices (Figure S7, Supporting Information), although for the particular region observed, the amorphous film did not extend through the whole film thickness, but only in the top region. The existence of the amorphous phase in the LRS suggests that the phase change is not reversible. The a-LSM50 could be observed by optical microscopy predominantly at edge of the Ti electrode facing the Pt electrode, and also on the adjacent edges. The volume of a-LSM50 seems to be related with the maximum voltage applied to the device, but the onset of the appearance and the voltage dependence could not be clearly determined. The existence of this a-LSM50 region close to the Ti electrode is expected to result in a smaller effective active region directly facing the Pt electrode, so a longer electronic path through the LSM film till the active Ti electrode is reached, and thus to an increased series resistance.

3. Discussion

The counter-clockwise *R-V* characteristics of the Pt/Ti/LSM50\Pt devices are in agreement with the drift of oxygen inducing the change of resistance of the device through a reversible solid-state redox reaction. The mobility of oxygen ions was already suggested in the pristine devices, where oxygen vacancies are expected to be formed in LSM50 due to the oxidation of Ti into TiO_x, and a slight change of oxygen content was found for the different resistance states (Figure 5). The reduction of LSM50 and simultaneous oxidation of Ti imply an increase of the materials' resistivity, and thus, a larger total resistance measured in the device. The opposite redox reaction decreases the resistivity of the redox pair and the device then shows a lower resistance. Indeed, when a large enough positive voltage is applied on the Ti electrode, the negatively charged oxygen ions would drift from LSM50 into Ti (/TiO_x), which reduces and oxidizes, respectively, causing the RESET of the device into the HRS. The application of negative voltage would result in the reincorporation of oxygen into LSM50 (oxidation) from the TiO_x electrode (reduction), leading to the SET of the device in a LRS state. The multilevel states observed would correspond to different oxidation states and/or modified volume of the redox pair (LSM50 and Ti) that has undergone the redox reaction. This phenomenological description was also applied in our previous work on $La_{0.8}Sr_{0.2}MnO_{3\pm\delta}$-based devices, where the devices showed interface-type switching with a gradual transition.[3] However, the LSM50 devices presented here show several abrupt changes of resistance during SET and voltage dependence. In the following, an extension of the phenomenological mechanism mentioned above is presented and sketched in **Figure 7**. In the pristine state (Figure 7a), the devices present a reduced layer of LSM50 (LSM50-δ) and a thin and homogeneous TiO_2 interlayer, which acts as a tunnel barrier, as reported for Ti/$Pr_{0.48}Ca_{0.52}MnO_3$ devices.[34] During the RESET operation, the TiO_2 layer (and TiO_x) will thicken as result of oxygen incorporation. However, given the presence of amorphous TiO_x and of extended defects in LSM50, it is reasonable to assume that the oxidation front in the Ti electrode would be inhomogeneous with a profile similar to a mountain range, as sketched in Figure 7b. In this scenario, the main conduction would occur through the valleys of the TiO_2 region which may also present different thicknesses. In the SET operation, schematized in Figure 7c, the overall oxidation of the Ti electrode will decrease. In particular, at small negative voltage, the thinner valleys (v_1 in Figure 7b) would vanish first, connecting locally the LSM50 and the Ti (TiO_x). As the negative voltage increases, the thicker valleys (v_2 in Figure 7b) will then connect. The different

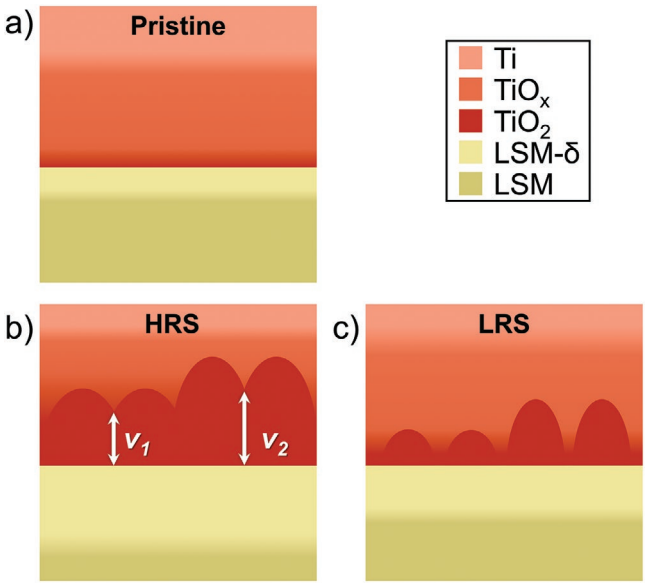

Figure 7. Sketch of the phenomenological model of the resistive switching in Pt/Ti/LSM50\Pt devices, describing the evolution of the Ti/LSM50 interface in a) pristine state, b) HRS and c) LRS.

thickness of the valleys would result in several drops of resistance at different voltages; exhibiting hence a multifilament-like behavior, as observed experimentally. The V_{set} dependence of the drops of resistance, can thus be explained as an overall thicker TiO_2 layer acting as tunable tunnel barrier. The presence of the inhomogeneous TiO_2 region is expected to be similar for the devices of all sizes. Nonetheless, the large devices will statistically present a larger number of "filaments", which will be connecting more gradually in comparison to the fewer number of "filaments" present in the small devices, resulting in the almost gradual SET observed in the *R-V* curves. The formation of the a-LSM50 region at the edge of the Ti electrode is in agreement with an oxygen drift, accumulation, and eventual O_2 gas formation, which would cause the microstructural voids observed. The presence of an a-LSM50 phase has shown not to be detrimental for the operation of the device and is expected to add a serial resistance smaller than the resistance of the two redox interlayers. It is reasonable to relate the formation of the a-LSM50 region to the initialization process, after which an irreversible increase in resistance has been measured. This increase is clearly visible by comparing the first five cycles at ±2 V of the pristine and initialized device (open and closed symbols for cycles 1 to 5 in Figure 4a). Nevertheless, a minor role of the a-LSM50 region in the redox process leading to the reversible resistance changes taking place in the device cannot be totally excluded.

In our previous work, we showed that the LSM20/LAO-based devices show reproducible and multilevel resistive switching, that was largely improved by the presence of dislocations.[3] The LSM20 devices required larger operating voltage and the HRS/LRS window was smaller, typically between 1.3 and 5 for V_{amp} = 4 to 20 V. In the present work, we exploited the easy formation of oxygen vacancies in LSM50 to obtain larger operating windows at smaller voltages, i.e., 2.1 to 184 for V_{amp} = 4 to 12 V. These results clearly show that it is possible to improve and optimize the memristive properties similar devices by modifying the Sr substitution of the manganite, leading to changes in ionic and electronic conductivity of the material.

4. Conclusion

In this work, we obtained resistive switching in epitaxial LSM50 for the first time. Epitaxial LSM50/LAO layers with extended microstructural defects were deposited by PI-MOCVD. The layer presents two types of domains with different out-of-plane crystal orientations (tetragonal structure), which can be related to the grain-like structure observed at the top surface. The EDS measurements of pristine Pt/Ti/LSM50\Pt planar memristive devices, together with the XANES, suggest that the formation of a TiO_x interlayer occurs during fabrication, concomitantly to the formation of oxygen vacancies in LSM50. The devices exhibit forming-free, multilevel, and reproducible resistive switching with good retention and better performance, compared to our previous study on epitaxial $La_{0.8}Sr_{0.2}MnO_{3\pm\delta}$ thin films. We propose a phenomenological description of the switching mechanism relying on the drift of oxygen across the Ti/LSM50 interface and the modification of the tunnel barrier in occurrence with the change of resistivity in LSM50. The abrupt resistance drops occurring during SET were attributed to thickness inhomogeneities of the tunnel barrier through the TiO_2 layer, which provide localized conduction paths. The electrical measurements and resistive switching description are in agreement with our previous work; from which we infer that the larger operating window (factor 40) and smaller operation voltage (40% smaller) observed in LSM50 compared to LSM20 is due to the easier formation of oxygen vacancies. Therefore, we have proven that the performance of memristive devices can be tuned and improved using more easily reducible compositions in combination with microstructures that facilitate oxygen migration toward the electrodes.

5. Experimental Section

Material Deposition: Epitaxial 21 nm thick $La_{0.5}Sr_{0.5}MnO_{3-\delta}$ (LSM50) films were grown by pulsed injection metal-organic chemical vapor deposition (PI-MOCVD) in a JIPELEC reactor described elsewhere.[15,46] The metal-organic precursors, $La(thd)_3$, $Sr(thd)_2$-tetraglyme, and $Mn(thd)_3$, [thd = 2,2,6,6,-tetramethyl-3,5-heptanedionato] were purchased from Strem Chemicals and were dissolved in m-xylene from Alfa Aesar. As an extension to the composition preliminary study,[3] the cationic concentration in the solution was optimized to grow films with 50% strontium substitution and [(La+Sr)/Mn] ratio close to 1. The total concentration of the solution was 22.5 mM, with [(La+Sr)/Mn] precursor ratio of 2.3 and [Sr/(La+Sr)] precursor ratio of 0.8. In the optimization study, the composition of the film deposited with the abovementioned solution composition yields films with [(La+Sr)/Mn]≈0.96 and [Sr/(La+Sr)]≈0.52.

The films were deposited on a 10 × 10 mm^2 single crystal of $LaAlO_3$ $(100)_{pc}$ (LAO) substrate purchased from Crystec. The solution was evaporated at 250 °C and the reaction chamber was heated up at 675 °C. The deposition pressure was 5 Torr and oxygen was added into the chamber with a partial pressure of 2 Torr. The gas flow rates were kept constant during deposition at 0.3 slm for O_2 and 0.4 slm for Ar. The liquid precursor solution was injected at 2.5 Hz with an opening time of 2 ms for 5000 pulses at a feeding rate of ≈0.29 mL min^{-1} using argon as

carrier gas. After the film growth, the samples were cooled down under Ar atmosphere.

Characterization: The orientation of the film and identification of the crystalline phases were studied by XRD in Bragg–Brentano θ-2θ configuration in a Bruker D8 Advance serie II diffractometer with Cu Kα1 radiation ($\lambda = 1.5406$ Å) equipped with rotating holder. The instrumental shift and displacement were corrected by aligning the LAO substrate peaks to their reference, ICDD-00-031-0022. SEM was performed in a FEG ZEISS GeminiSEM 300 to study the surface morphology. AFM topography scans were performed in a Bruker Icon AFM in tapping mode to analyze the grain size and roughness of the film. Cross-sectioned TEM samples were prepared by automated polishing, using a MultiPrepTM system (Allied High Tech Products Inc.). The final polishing was performed using a felt-covered disc impregnated with a silica solution until the appearance of the first extinction fringe among those of equal thickness. Ar-milling was then used to reduce the total thickness. These samples were observed at 200 kV in a JEOL JEM 2010 LaB6 TEM (with a resolution of ≈0.19 nm). Complementary, the electron transparent lamellas for TEM cross-section analysis of the devices were obtained by Focused Ion Beam milling using a FEI dual-beam Helios 450S. A platinum layer was sputtered to prevent damage from the ion beam consisting in rough milling at 30 kV operating voltage followed by a fine milling at 2–8 kV. The lamellas were observed at 200 kV in a Tecnai Osiris FEI microscope equipped with a Super-X detector for Energy Dispersive X-ray (EDS) spectroscopy.

The Mn oxidation state of $La_{0.8}Sr_{0.2}MnO_{3\pm\delta}$ films was probed by X-ray Absorption Near Edge Spectroscopy (XANES) at the Mn K-edge in ID12 beamline at European Radiation Synchrotron Facilities (ESRF) under the project number MA-4802 (DOI of data: 10.15151/ESRF-ES-445198462). The measurements were carried out at 298 K and atmospheric pressure, using a nearly round beam spot size of 5 µm, and the fluorescence signal was collected. The absorption energy of the Mn K-edge was determined as the maximum of the first derivative for each spectrum. A Mn88Ni12 alloy sample was used as a standard and the energy position of the Mn K-edge was calibrated at 6539.05 eV.

Device Fabrication and Characterization: The microfabrication of planar devices was performed in the PTA cleanroom facilities (Grenoble). The mask design included: (i) facing Ti and Pt square electrodes of different sizes (100^2, 200^2, 300^2, and 400^2 µm^2) separated 50 µm; and (ii) 2000×200 µm^2 Pt electrodes at different distances for transmission line measurements (TLM). Laser-assisted lithography (µPG 101 from HEIDELBERG Instruments) and electron-beam induced metal evaporator (MEB550 from PLASSYS) were used to transfer the mask design on the sample. The exposed surface of the sample was mildly etched using Ar^+ to enhance metal adhesion and remove potential residues of the photoresist. Pt (≈100 nm thick) was used as a counter electrode, and Ti (≈10 nm) capped with Pt (≈90 nm) to prevent atmospheric oxidation was selected as active electrode. The electrodes were evaporated in high vacuum conditions (≈10^{-8} mbar) on top of the LSM50 thin film sample, forming planar devices. Devices formed by 200×200 µm^2 electrodes and separated by 50 µm are referred to as standard devices.

The current-voltage ($I(V)$) characteristics were obtained in ambient conditions using a Keithley 4200A-SCS semiconductor characterization system in voltage-control mode. Two tungsten probes (tip radius 10 µm) were used to contact the devices. All measurements were performed applying voltage on Pt/Ti electrode and grounding the Pt counter electrode. The bipolar sweeps followed the sequence: 0 V → $+V_{amp}$ → 0 V → $-V_{amp}$ → 0 V. The resistance of the device was obtained from the writing voltage curve at -1 V. The retention measurements were carried out at room temperature and the resistance was measured at +0.1 V by DC sweeps, in the case of HRS_{10V} and LRS_{10V}, every 30 s for the first hour, and then every 5–8 min for the remaining time of measurement. The resistance of HRS_{12V} and LRS_{12V}, was measured every 30 s. Before each retention measurement, the device was cycled five times at the assessed voltage amplitude (either 10 V or 12 V) to stabilize the response. We note that after one full cycle the device switches into HRS and is left in the LRS, hence, an additional positive half cycle was required to switch and measure the stability of HRS.

Supporting Information

Supporting Information is available from the Wiley Online Library or from the author.

Acknowledgements

This work has been supported by the ANR funded project "Mangaswitch" (ANR-17-CE24-0038) and has benefited from characterization equipment of the Grenoble INP – CMTC platform supported by the Centre of Excellence of Multifunctional Architectured Materials "CEMAM" n°ANR-10-LABX-44-01 funded by the "Investments for the Future" Program, and from the "Plateforme Technologique Amont" of Grenoble, with the financial support of the "Nanosciences aux limites de la Nanoélectronique" Fundation and CNRS Renatech network. In addition, part of this work, carried out on the Platform for NanoCharacterisation (PFNC) of CEA, was supported by the "Recherche Technologique de Base" program of the French National Research Agency (ANR). The authors thank Eirini Sarigiannidou for fruitful discussions on the TEM imaging.

Conflict of Interest

The authors declare no conflict of interest.

Data Availability Statement

The data that support the findings of this study are openly available in Zenodo at https://doi.org/10.5281/zenodo.7462516, reference number 7462516.

Keywords

epitaxial thin films, manganites, memristive devices, metal-organic chemical vapor deposition (MOCVD), oxygen vacancies, resistive switching, valence change memories (VCMs)

Received: December 20, 2022
Revised: February 28, 2023
Published online: April 18, 2023

[1] "International Roadmap for Devices and Systems: Beyond CMOS and Emerging Materials Integration," can be found under https://irds.ieee.org/editions/2022 (accessed: December 2022).
[2] S. Parveen, L. T. Manamel, A. Mukherjee, S. Sagar, B. C. Das, *Adv. Mater. Interfaces* **2022**, *9*, 2200562.
[3] C. Moncasi, G. Lefèvre, Q. Villeger, L. Rapenne, H. Roussel, A. Bsiesy, C. Jiménez, M. Burriel, *Adv. Mater. Interfaces* **2022**, *9*, 2200498.
[4] A. Asamitsu, Y. Tomioka, H. Kuwahara, Y. Tokura, *Nature* **1997**, *388*, 50.
[5] A. Urushibara, Y. Moritomo, T. Arima, A. Asamitsu, *Phys. Rev. B* **1995**, *51*, 14103.
[6] L. Yao, S. Inkinen, S. van Dijken, *Nat. Commun.* **2017**, *8*, 14544.
[7] R. Waser, R. Dittmann, C. Staikov, K. Szot, *Adv. Mater.* **2009**, *21*, 2632.
[8] K. Szot, W. Speier, G. Bihlmayer, R. Waser, *Nat. Mater.* **2006**, *5*, 312.
[9] M. Janousch, G. I. Meijer, U. Staub, B. Delley, S. E. Karg, B. P. Andreasson, *Adv. Mater.* **2007**, *19*, 2232.
[10] C. Moreno, C. Munuera, S. Valencia, F. Kronast, X. Obradors, C. Ocal, *Nano Lett.* **2010**, *10*, 3828.

[11] T. K. Khuu, G. Lefèvre, C. Jiménez, H. Roussel, A. Riaz, S. Blonkowski, E. Jalaguier, A. Bsiesy, M. Burriel, *Adv. Mater. Technol.* **2022**, *7*, 2200329.
[12] M. Huang, M. Schwacke, M. Onen, J. del Alamo, J. Li, B. Yildiz, *Adv. Mater.* **2022**, 2205169.
[13] A. Gutsche, S. Siegel, J. Zhang, S. Hambsch, R. Dittmann, *Front Neurosci* **2021**, *15*, 1.
[14] B. Meunier, D. Pla, R. Rodriguez-Lamas, M. Boudard, O. Chaix-Pluchery, E. Martinez, N. Chevalier, C. Jiménez, M. Burriel, O. Renault, *ACS Appl. Electron. Mater.* **2019**, *1*, 675.
[15] R. Rodriguez-Lamas, D. Pla, O. Chaix-Pluchery, B. Meunier, L. Rapenne, H. Roussel, X. Mescot, F. Wilhelm, A. Rogalev, M. Boudard, Q. Rafhay, C. Jiménez, M. Burriel, *Beilstein J. Nanotechnol.* **2019**, *10*, 389.
[16] B. Meunier, E. Martinez, R. Rodriguez-Lamas, D. Pla, M. Burriel, C. Jimenez, Y. Yamashita, O. Renault, *ACS Appl. Electron. Mater.* **2021**, *3*, 5555.
[17] B. Meunier, E. Martinez, R. Rodriguez-Lamas, D. Pla, M. Burriel, M. Boudard, C. Jiménez, J. P. Rueff, O. Renault, *J. Appl. Phys.* **2019**, *126*, 225302.
[18] F. Chiabrera, I. Garbayo, L. López-Conesa, G. Martín, A. Ruiz-Caridad, M. Walls, L. Ruiz-González, A. Kordatos, M. Núñez, A. Morata, S. Estradé, A. Chroneos, F. Peiró, A. Tarancón, *Adv. Mater.* **2018**, *31*, 1805360.
[19] F. M. Chiabrera, F. Baiutti, J. M. Börgers, G. F. Harrington, L. Yedra, M. O. Liedke, J. Kler, P. Nandi, J. de Dios Sirvent, J. Santiso, M. López-Haro, J. J. Calvino, S. Estradé, M. Butterling, A. Wagner, F. Peiró, R. A. de Souza, A. Tarancón, *JPhys Energy* **2022**, *4*, 044011.
[20] F. Chiabrera, I. Garbayo, D. Pla, M. Burriel, F. Wilhelm, A. Rogalev, M. Núñez, A. Morata, A. Tarancón, *APL Mater.* **2019**, *7*, 013205.
[21] J. M. Börgers, J. Kler, K. Ran, E. Larenz, T. E. Weirich, R. Dittmann, R. A. de Souza, *Adv. Funct. Mater.* **2021**, *31*, 2105647.
[22] J. Mizusaki, Y. Yonemura, H. Kamata, K. Ohyama, N. Mori, H. Takai, H. Tagawa, M. Dokiya, K. Naraya, T. Sasamoto, H. Inaba, T. Hashimoto, *Solid State Ionics* **2000**, *132*, 167.
[23] S. P. Jiang, *J. Mater. Sci.* **2008**, *43*, 6799.
[24] S. Carter, A. Selcuk, R. J. Chater, J. Kajda, J. A. Kilner, B. C. H. Steele, *Solid State Ionics* **1992**, *53*, 597.
[25] N. Lee, Y. Lansac, H. Hwang, Y. H. Jang, *RSC Adv.* **2015**, *5*, 102772.
[26] O. Tripathy, P. P. Kumar, *J. Mater. Sci.* **2017**, *52*, 6542.
[27] R. A. de Souza, J. A. Kilner, J. F. Walker, *Mater. Lett.* **2000**, 43.
[28] R. A. de Souza, J. A. Kilner, *Solid State Ionics* **1998**, *106*, 175.
[29] H. K. Lee, *Mater. Chem. Phys.* **2002**, *77*, 639.
[30] J. Hemberger, A. Krimmel, T. Kurz, H. A. Krug von Nidda, V. Y. Ivanov, A. A. Mukhin, A. M. Balbashov, A. Loidl, *Phys Rev B Condens Matter Mater Phys* **2002**, *66*, 094410.
[31] A. Sawa, R. Meyer, in *Resistive Switching: From Fundamentals of Nanoionic Redox Processes to Memristive Device Applications* (Eds.: D. Ielmini, R. Waser), Wiley-VCH, Weinheim **2016**, pp. 457–482.
[32] S. G. Choi, H. S. Lee, H. Choi, S. W. Chung, H. H. Park, *Thin Solid Films* **2013**, *529*, 352.
[33] S. Asanuma, H. Akoh, H. Yamada, A. Sawa, *Phys. Rev. B Condens. Matter Mater. Phys.* **2009**, *80*, 235113.
[34] A. Herpers, C. Lenser, C. Park, F. Offi, F. Borgatti, G. Panaccione, S. Menzel, R. Waser, R. Dittmann, *Adv. Mater.* **2014**, *26*, 2730.
[35] F. Borgatti, C. Park, A. Herpers, F. Offi, R. Egoavil, Y. Yamashita, A. Yang, M. Kobata, K. Kobayashi, J. Verbeeck, G. Panaccione, R. Dittmann, *Nanoscale* **2013**, *5*, 3954.
[36] A. Sawa, T. Fujii, M. Kawasaki, Y. Tokura, *Appl. Phys. Lett.* **2004**, *85*, 4073.
[37] K. Maas, E. Villepreux, D. Cooper, E. Salas-Colera, J. Rubio-Zuazo, G. R. Castro, O. Renault, C. Jimenez, H. Roussel, X. Mescot, Q. Rafhay, M. Boudard, M. Burriel, *Adv. Funct. Mater.* **2020**, *30*, 1909942.
[38] K. Maas, E. Villepreux, D. Cooper, C. Jiménez, H. Roussel, L. Rapenne, X. Mescot, Q. Rafhay, M. Boudard, M. Burriel, *J. Mater. Chem. C Mater.* **2020**, *8*, 464.
[39] R. Dittmann, S. Menzel, R. Waser, *Adv. Phys.* **2022**, *70*, 155.
[40] E. Navickas, Y. Chen, Q. Lu, W. Wallisch, T. M. Huber, J. Bernardi, M. Stöger-Pollach, G. Friedbacher, H. Hutter, B. Yildiz, J. Fleig, *ACS Nano* **2017**, *11*, 11475.
[41] H. C. Pan, C. C. Chou, H. L. Tsai, *Appl. Phys. Lett.* **2003**, *83*, 3156.
[42] B. Gharbage, F. Mandier, H. Lauret, C. Roux, T. Pagnier, *Solid State Ionics* **1995**, *82*, 85.
[43] S. K. Chaluvadi, F. Ajejas, P. Orgiani, S. Lebargy, A. Minj, S. Flament, J. Camarero, P. Perna, L. Méchin, *J. Phys. D Appl. Phys.* **2020**, *53*, 375005.
[44] C. Adamo, X. Ke, H. Q. Wang, H. L. Xin, T. Heeg, M. E. Hawley, W. Zander, J. Schubert, P. Schiffer, D. A. Muller, L. Maritato, D. G. Schlom, *Appl. Phys. Lett.* **2009**, *95*, 112504.
[45] Y. Konishi, M. Kasai, M. Izumi, M. Kawasaki, Y. Tokura, *Mater. Sci. Eng. B Solid State Mater. Adv. Technol.* **1998**, *56*, 158.
[46] J. P. Sénateur, F. Felten, S. Pignard, F. Weiss, A. Abrutis, V. Bigelyte, A. Teiserskis, Z. Saltyte, B. Vengalis, *J. Alloys Compd.* **1997**, *251*, 288.